Journal of
Polymer Materials

Tech Science Press

http://doi.org/10.32604/jpm.2026.087360

ARTICLE

Segmental Dynamics, Ion-Associated Relaxation, and Ion Transport in Cellulose-Based Gel Polymer Electrolytes Revealed by Broadband Dielectric Spectroscopy

Ruoxi Zhang[1], Rongzu Sun[1], Wei Zhou[2,*] and Zhen Chen[1,*]

[1]Department of Applied Chemistry, School of Materials and Chemistry, Anhui Agricultural University, Hefei, China
[2]School of Light Industry Science and Engineering, Beijing Technology and Business University, Beijing, China
*Corresponding Authors: Wei Zhou. Email: zhouw@th.btbu.edu.cn; Zhen Chen. Email: zchen@ahau.edu.cn

Received: 15 June 2026; Accepted: 14 September 2026; Published: 24 September 2026

ABSTRACT: Cellulose-based gel polymer electrolytes (GPEs) are promising sustainable candidates for next-generation lithium batteries; however, the relationship between polymer dynamics and ion transport remains insufficiently understood. In this study, cellulose-based GPEs with varying lithium salt concentrations and crosslinking densities were systematically investigated using broadband dielectric spectroscopy, complemented by structural and thermal characterizations. Three dielectric relaxations including a secondary β relaxation, a structural α relaxation arising from cooperative segmental motion of the cellulose network, and a slower near-Debye α' relaxation were identified. Both the α and α' processes follow Vogel–Fulcher–Tammann (VFT) behavior, indicating their strong coupling with the glassy dynamics of the polymer matrix. The α' process is plausibly ascribed to orientational polarization of ion-associated species, such as transient ion pairs or small ionic aggregates coordinated with the cellulose network. The direct current conductivity of the samples was also found following VFT behavior. Notably, the conductivity relaxation time nearly coincides with the α relaxation time across the entire investigated temperature range for all compositions, suggesting that lithium-ion transport is predominantly governed by polymer segmental dynamics. The dielectric glass transition temperature and fragility index, derived from VFT analysis, exhibit marked dependencies on salt concentration and crosslinking density, whereas the calorimetric glass transition temperature remains virtually invariant. This work unveils a strongly coupled ion-transport mechanism and provides fundamental insights into the intricate interplay among polymer dynamics, ionic association, and charge transport in cellulose-based GPEs.

KEYWORDS: Gel polymer electrolyte; dielectric spectroscopy; lithium batteries; solid-state electrolyte; direct current conductivity; structural relaxation

1 Introduction

Driven by the growing global demand for efficient and sustainable energy storage systems, lithium-ion batteries and supercapacitors have attracted extensive attention owing to their outstanding electrochemical performance [1,2]. As a core constituent of these systems, electrolytes have persistently remained a central focus of research endeavors [3]. Conventional liquid electrolytes (LEs), however, pose significant safety risks, such as leakage, combustion, and even explosion, which severely hinder their application in next-generation high-energy-density devices [4,5]. To address these safety concerns, solid-state electrolytes (SEs) have emerged as promising alternatives and attracted tremendous interest in recent years [6,7].

SEs are conventionally categorized into all-solid-state electrolytes (ASEs) and gel polymer electrolytes (GPEs) [8]. Though ASEs completely eliminate liquid components, their practical application is largely

limited by suboptimal electrode/electrolyte interfacial compatibility, elevated interfacial resistance, and restricted ionic mobility, often associated with lithium dendrite formation [7,9,10]. In comparison, GPEs, generally consisting of a polymer matrix, lithium salt, and plasticizer, represent a unique quasi-solid system that synergistically integrates the merits of both LEs and ASEs [8,11,12]. On one hand, they retain relatively high ionic conductivity and excellent interfacial wettability similar to LEs; on the other hand, the polymer framework provides mechanical robustness and improved safety [8,11,13]. This combination enables GPEs to reconcile electrochemical efficacy and operational reliability, positioning them as compelling candidates for next-generation energy storage materials [11–14]. Nevertheless, conventional GPEs predominantly employ fossil-derived polymers as the matrix, which are often flammable, toxic, or costly, thus conflicting with the principles of green and sustainable chemistry [15,16]. Accordingly, the design and deployment of environmentally benign and renewable materials for GPEs have emerged as a pivotal research frontier [15].

Among various green alternatives to fossil-derived polymers, cellulose and its derivatives have garnered significant attention due to their natural abundance, inherent biodegradability, and unique molecular architecture [15–18]. As the most abundant natural polymer, cellulose features a dense distribution of hydroxyl groups capable of coordinating with Li^+ ions, thereby facilitating lithium salt dissociation and enhancing ion transport. Meanwhile, the extensive hydrogen-bonding network endows it with excellent mechanical properties, making it an ideal matrix for constructing robust GPEs. Recent studies have demonstrated that cellulose-based GPEs can achieve high ionic conductivity and stable electrochemical performance, highlighting their considerable promise as viable, eco-friendly alternatives to conventional petroleum-based electrolyte systems [18–20].

To date, significant progress has been achieved in cellulose-based GPEs, particularly in improving ionic conductivity through compositional optimization and porous structure design [20,21]. Nevertheless, the fundamental mechanistic understanding of ion transport within these systems still remains insufficient. It is generally accepted that ionic conduction in GPEs is intrinsically coupled with polymer segmental dynamics, ion–matrix interactions, and microstructural features [22,23]. Therefore, elucidating the structure–property relationships linking composition, microstructure, and macroscopic electrochemical performance is crucial for rational design of advanced materials. In this context, dielectric and impedance spectroscopy techniques have been widely used to probe charge transport behavior in polymer electrolytes [24,25] and specifically in GPEs [26–28]. Previous studies on cellulose-based systems have primarily focused on ionic conductivity and electrode polarization, while recent works have employed complementary techniques, such as NMR and spectroscopic analyses, to unravel ion dynamics. These studies collectively suggest that ion transport in cellulose-based matrices is critically modulated by polymer chain mobility and network architecture. However, dielectric investigations on cellulose-based GPEs still remain relatively limited; in particular, comprehensive investigations utilizing broadband dielectric spectroscopy (BDS) to resolve multi-scale relaxation processes—such as segmental (α) relaxation, ion hopping, and electrode polarization—are still scarce [24,29]. Moreover, although the individual effects of crosslinking structure or lithium salt concentration have been examined, their synergistic influence on dielectric relaxation behavior and ion transport mechanisms has rarely been systematically addressed. Consequently, the intrinsic correlations among polymer network structure, segmental dynamics, and ionic conduction in cellulose-based GPEs remain inadequately resolved.

In this work, a series of cellulose-based GPEs with varying crosslinking density and salt concentration were prepared, which were systematically characterized using X-ray diffraction (XRD), scanning electron microscopy (SEM), Fourier-transform infrared spectroscopy (FTIR), differential scanning calorimetry (DSC), and broadband dielectric spectroscopy (BDS). This work aims to elucidate the influence of crosslinking density and salt content on the microstructure, segmental dynamics, and lithium-ion transport of the

cellulose-based GPEs, thereby contributing to a deeper insight into the structure–property relationship and providing guidance for the design of high-performance, eco-friendly polymer electrolytes.

2 Experiments and Methods

2.1 Materials

Sodium Hydroxide (NaOH, 96%) and urea ($CO(NH_2)_2$, 99%) were purchased from Xilong Science Co., Ltd. Cellulose powder (99%) was purchased from Shanghai Jingchun Biochemical Technology Co., Ltd. Bistrifluoromethane sulfonimide lithium (LiTFSI, 99%) and epichlorohydrin (C_3H_5ClO, ECH, 99.5%) were purchased from Macklin Biochemical Technology Co., Ltd. All chemicals were used as received.

2.2 Preparation of Cellulose-Based GPE Films

To fabricate the cellulose-based GPEs, transparent cellulose solutions were initially prepared. Specifically, 2 g of cellulose powder was slowly added into 50 mL of an aqueous NaOH/urea solution (6:4:90 by weight) under continuous stirring, followed by incubation at −5°C for 12 h. The resulting mixture was then vigorously stirred at room temperature until complete dissolution of the cellulose powder and subsequently centrifuged at 7200 rpm for 15 min to remove residual insoluble impurities.

The GPE films were prepared via a solution casting method. Certain amounts of LiTFSI and ECH were successively introduced into the as-prepared cellulose solution and stirred for 30 min to ensure homogeneity. The resultant solutions were then cast into Petri dishes and heated at 60°C for 2 h to facilitate crosslinking and gelation. Subsequently, the freestanding GPE films were peeled off and immersed in ethanol for 12 h to remove unreacted residues, followed by drying in a forced-air convection oven at 60°C for 30 min. Two series of films were prepared (formulations summarized in Table S1). In series 1 (GPE-1, GPE-2, and GPE-3), the crosslinking density was maintained constant, while the molar ratio of LiTFSI to anhydroglucose unit (AGU) ($n_{Li^+} : n_{AGU}$) was varied from 0.5 to 1.5 in increments of 0.5. In series 2 (GPE-4, GPE-2, and GPE-5), $n_{Li^+} : n_{AGU}$ was fixed and the crosslinking density was adjusted from 4% to 6%.

2.3 SEM Measurement

The morphology and microstructural characteristics of the GPE samples were characterized using a HITACHI S-4800 (Hitachi, Japan) field-emission SEM. The specimens were prepared by mounting a small section of the sample onto conductive carbon tape, followed by gold sputter-coating for 60 s using an ion sputtering system. Imaging was performed at an accelerating voltage ranging from 0.5 to 30 kV, with representative micrographs acquired at optimized magnifications.

2.4 FTIR Measurement

The FTIR measurements were performed using a FT/IR-4X spectrometer (Jasco, Japan) equipped with a mid-infrared deuterated L-alanine-doped triglycine sulfate (DLaTGS) detector and a broad-range beam-splitter, which enables measurements over an extended wavenumber range of 7800 to 350 cm^{-1}. Spectral data were acquired over this range. All samples were measured in triplicate, and subsequent data processing, including baseline correction and background subtraction, was performed using the instrument's proprietary software.

2.5 DSC Measurement

The DSC measurements were conducted using a HITACHI DSC200 (Hitachi, Japan) under a controlled nitrogen atmosphere. The samples were cooled from room temperature to −80°C at a rate of 20°C/min and isothermally held for 10 min, followed by heating to 100°C at a rate of 20°C/min.

2.6 XRD Measurement

The XRD measurements were carried out by using a Bruker D8 Advance X-ray diffractometer (Bruker, Germany) equipped with a Cu $K\alpha$ radiation source. Data were collected over a 2θ range of 5° to 90° with a scanning speed of 2°/min.

2.7 Dielectric Measurements

The BDS measurements were carried out using a Broadband Dielectric Spectrometer Concept 40 (Novocontrol GmbH, Germany), equipped with a high-precise temperature controller (Quatro Cryosystem) with a controlling accuracy better than 0.05°C. The GPE films were sandwiched between two gold-plated copper electrodes with a diameter of 10 mm, and then mounted into a sample holder (Novocontrol BDS 1200). The thickness of the films was precisely determined after the dielectric measurements. The dielectric measurements were performed in a frequency range of 0.1 Hz to 10 MHz, and the temperature was varied from −60°C to 20°C in steps of 5°C.

2.8 Dielectric Spectra Analysis

Since the dielectric responses of the GPE films contain several superimposed dielectric relaxations and are influenced by electrode polarization (EP) and direct current (DC) conductivity σ_{DC}, the following fitting function was employed to quantitatively analyze the spectra of complex permittivity ($\varepsilon^* = \varepsilon' - i\varepsilon''$ with ε' and ε'' being the dielectric constant and dielectric loss, respectively), which contains a sum of several Havriliak-Negami (HN) [30] terms plus two more terms accounting for σ_{DC} and EP effect

$$\varepsilon^*(\omega) = \varepsilon_\infty + \sum_j \frac{\Delta\varepsilon_j}{\left[1 + (i\omega\tau_{HN\,j})^{\beta_{HN\,j}}\right]^{\gamma_{HN\,j}}} + \frac{\sigma_{DC}}{i\omega\varepsilon_0} + a\omega^{-b} \tag{1}$$

where ε_∞ is the high-frequency limit of dielectric constant, ε_0 is the permittivity of vacuum, $\Delta\varepsilon$ is the relaxation strength, τ_{HN} is the characteristic relaxation time, β_{HN} ($0 < \beta_{HN} \leq 1$) and γ_{HN} ($0 < \gamma_{HN} \leq 1$) are the parameters describing the symmetric and asymmetric broadening of the relaxation peak, respectively (when $\gamma_{HN} = 1$, the HN function becomes Cole-Cole function), j is the number of dielectric relaxations, and the term $a\omega^{-b}$ represents the EP effect with a and b being fitting variables. The maximum relaxation time (or most probable relaxation time) τ_{max} is correlated with τ_{HN} as [30].

$$\tau_{max} = \tau_{HN} \times \sin^{1/\beta_{HN}}\left(\frac{\beta_{HN}\gamma_{HN}\pi}{2 + 2\gamma_{HN}}\right) \times \sin^{-1/\beta_{HN}}\left(\frac{\beta_{HN}\pi}{2 + 2\gamma_{HN}}\right) \tag{2}$$

To improve the resolution of the superimposed relaxations, the logarithmic derivative (LD) method [31] was employed to transform ε' into a derivative dielectric loss (ε''_{LD}), which is based on the Kramers-Kronig relationship and can be expressed as

$$\varepsilon''_{LD} = -\frac{\pi}{2}\frac{\partial\varepsilon'}{\partial \ln\omega} \approx \varepsilon''_{Rel} \tag{3}$$

where ω ($= 2\pi f$) is angular frequency, and $\varepsilon''_{\mathrm{Rel}}$ is the measured dielectric loss free of σ_{DC}.

3 Results and Discussion

3.1 Structural, Compositional, and Thermal Properties

Fig. 1 displays the digital photographs of the as-prepared GPE films (insets) and their corresponding micro-morphologies characterized via SEM. The optical images reveal that all samples form flexible and free-standing films without obvious macroscopic phase separation or electrolyte leakage, thereby demonstrating good compatibility between the crosslinked cellulose matrix and the lithium electrolyte. The SEM observations further elucidate their composition-dependent microstructures. GPE-1 and GPE-2 exhibit relatively rough and heterogeneous surface topographies characterized by locally aggregated domains, whereas GPE-3 and GPE-5 show smoother and more continuous morphologies, suggesting improved compatibility and homogenization within the polymer matrix. In contrast, GPE-4 displays numerous microscale pores or void-like structures, presumably arising from localized phase segregation or partial salt precipitation during solvent evaporation. Overall, these findings indicate that stable cellulose-based electrolyte networks were successfully constructed across all investigated formulations.

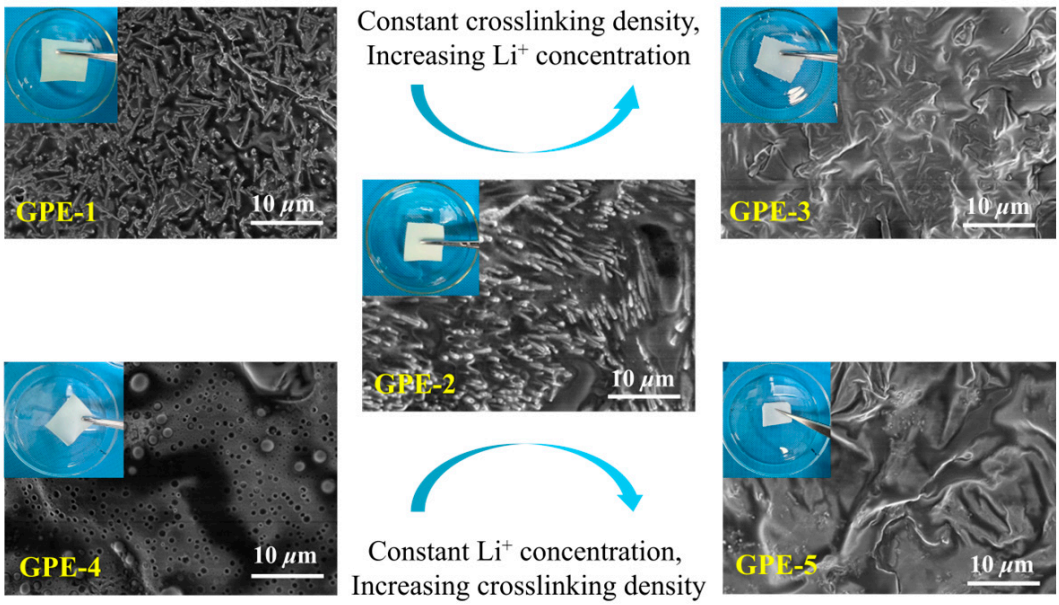

Figure 1: SEM images of cellulose-based GPE films with different Li^+ ion concentration and crosslinking density. The insets are the digital photographs of the corresponding samples.

The structural characteristics of the GPE samples were further investigated by XRD, FTIR, and DSC measurements, as demonstrated in Fig. 2. The XRD patterns (Fig. 2a) are mainly dominated by broad, diffused halos centered at $2\theta \approx 20^{\circ}$, indicative of the predominantly amorphous nature of the prepared GPEs, which is a typical feature of highly disordered cellulose-based materials with limited long-range crystalline order [32,33]. However, several sharp Bragg diffraction peaks emerge at higher scattering angles, implying the presence of trace amounts of partially recrystallized salt species. These reflections, specifically at 2θ values of approximately 31.7°, 45.5°, and 56.5°, are also discernible in ECH-crosslinked cellulose free of LiTFSI (Fig. S1), and can be indexed to the (200), (220), and (222) crystallographic planes of NaCl [34]. Therefore, the recrystallized phase should be assigned to NaCl rather than LiTFSI; the NaCl is presumed to form as a byproduct during the ECH crosslinking reaction in the NaOH-based solvent system. Since no

characteristic peaks corresponding to crystalline LiTFSI were detected, the lithium salt is believed to be completely dissociated and uniformly distributed within the crosslinked cellulose matrix.

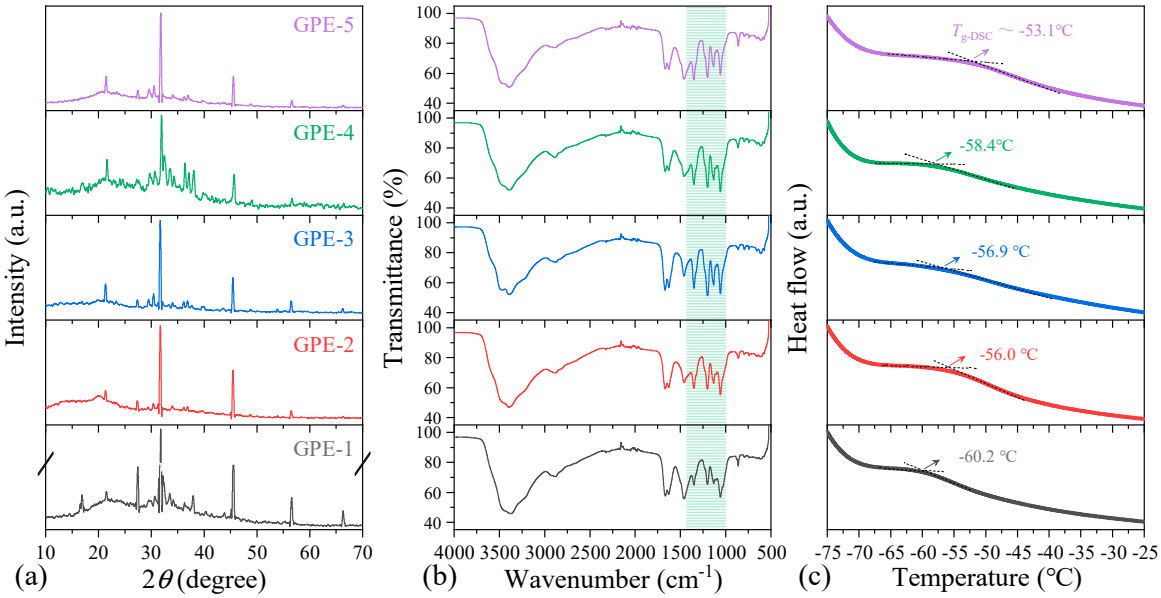

Figure 2: Structural and thermal characterizations of the cellulose-based GPE samples. (**a**) XRD patterns; (**b**) FTIR spectra; and (**c**) DSC curves.

The FTIR spectra (Fig. 2b) provide additional evidence for the successful incorporation and coordination of the lithium salt within the cellulose network. The spectra show characteristic absorption bands of the polymer host. Notably, shifts and changes in the intensity of the vibrational bands associated with polar functional groups (e.g., C-O/C-O-C stretching modes, highlighted in the shaded region) provide clear evidence of coordination interactions between the lithium ions and the polymer chains. This confirms that the lithium salt is not merely physically dispersed but is chemically integrated into the cellulose network through ion-dipole interactions. The calorimetric glass transition temperature ($T_{g\text{-}DSC}$) of the GPEs was determined by DSC, using the onset of the step change in heat flow as the characteristic transition point (Fig. 2c). All well below room temperature, the measured $T_{g\text{-}DSC}$ values are within a relatively narrow temperature range (approximately −60 to −53°C), and no clear dependence on either crosslinking density or lithium salt concentration was observed. The absence of a pronounced $T_{g\text{-}DSC}$ shift implies that the competing effects of ionic coordination, plasticization, and crosslinking may partially compensate one another within the present composition range.

3.2 Dielectric Relaxation Behavior

Fig. 3 shows the dielectric relaxation behavior of GPE-1 at the investigated temperatures, in terms of frequency dependent ε' (a), ε'' (b), ε''_{LD} (c), and σ' (d). As demonstrated in Fig. S2, the dielectric relaxation behaviors of the other samples are similar to that of GPE-1. As can be seen, although the dielectric relaxation behavior is dominated by strong EP and large σ_{DC}, dielectric relaxations can still be observed throughout the whole investigated temperature range.

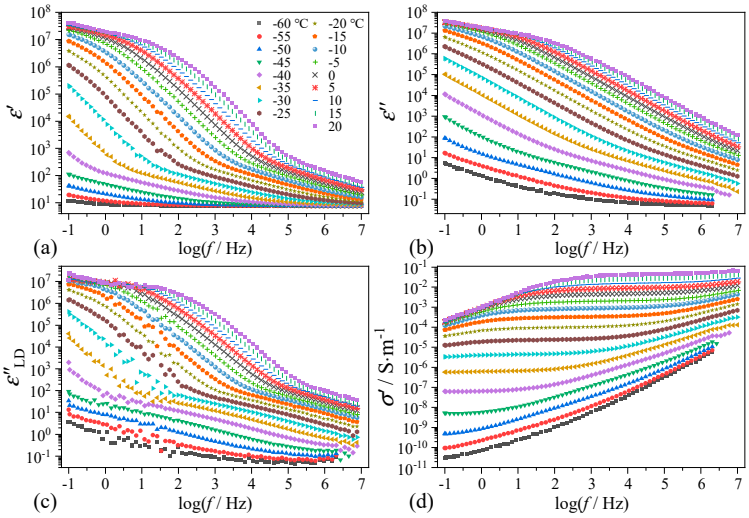

Figure 3: Frequency dependent dielectric constant (**a**), dielectric loss (**b**), derivative dielectric loss (**c**), and real conductivity (**d**) of GPE-1 at different temperatures.

To capture the features of these relaxations, all dielectric spectra were analyzed in line with Eq. (1). As representatives, Fig. 4 shows the fittings on the ε', ε'', $\varepsilon''_{\mathrm{LD}}$, and σ' spectra of GPE-1 at two selected temperatures (−40°C and −20°C), based on a simultaneous fitting procedure described in Refs. [35,36]. As demonstrated, the dielectric relaxation behavior of the GPE films is characterized by three main dielectric relaxations. The slowest relaxation (α' relaxation in Fig. 4) exhibits a near-Debye character, as evidenced by its symmetric shape and the β_{HN} value being close to unity (mostly greater than 0.8, indicative of a narrow relaxation time distribution). These features suggest this relaxation should not be a result of the segmental motion of the crosslinked cellulose network. On the other hand, since cellulose is not a Type-A polymer in a dielectric sense, especially crosslinked by ECH, this relaxation cannot be attributed to the normal mode relaxation either. Considering the extensive ion-polymer coordination structure formed between Li^+ ions and polar oxygen-containing groups of the cellulose network, it could be due to the orientational polarization of ion-associated species, such as contact ion pairs (Cellulose-O···Li^+···$TFSI^-$), triple ions (Cellulose-O···Li^+···$TFSI^-$···Li^+), or small ionic aggregates $(LiTFSI)_n$ that are uniformly dispersed in the amorphous network. However, this relaxation may also arise from interfacial polarization (the Maxwell-Wagner effect [37,38]) if microphase separation exists, which is often of Debye type and whose relaxation time generally follows the Arrhenius law [24]. With highly stretched and broad relaxation shape, the intermediate relaxation (α relaxation) exhibits typical structural relaxation characteristics of polymers [24], which is thereby most likely attributed to the cooperative motion of the segments of the crosslinked cellulose. The fastest relaxation (β relaxation) exhibits a symmetric and broad relaxation pattern, which is a typical secondary relaxation of polymers arising from localized side-group motions. For GPE-1, the β relaxation shifts outside of the investigated frequency window when T > −35°C. For GPE-3 (highest salt concentration) and GPE-4 (lowest crosslinking density), this relaxation was observed beyond the frequency window even when T > −50°C. This implies that elevated salt concentrations and reduced crosslinking densities facilitate side-group mobility, possibly attributed to the increase in free volume around the side groups (the influences of salt concentration and crosslinking density on the chain dynamics are discussed in detail below). The EP effect manifests itself as a linear dependence of logarithmic ε' and $\varepsilon''_{\mathrm{LD}}$ on log$f$ at low frequencies, as shown in Fig. 4a and Fig. 4c, respectively. The σ_{DC} in its logarithmic

form exhibits a linear dependence on log$f$ with a slope of −1 in the ε'' plot (Fig. 4b) and corresponds to the low-frequency platform in the σ' plot (Fig. 4d).

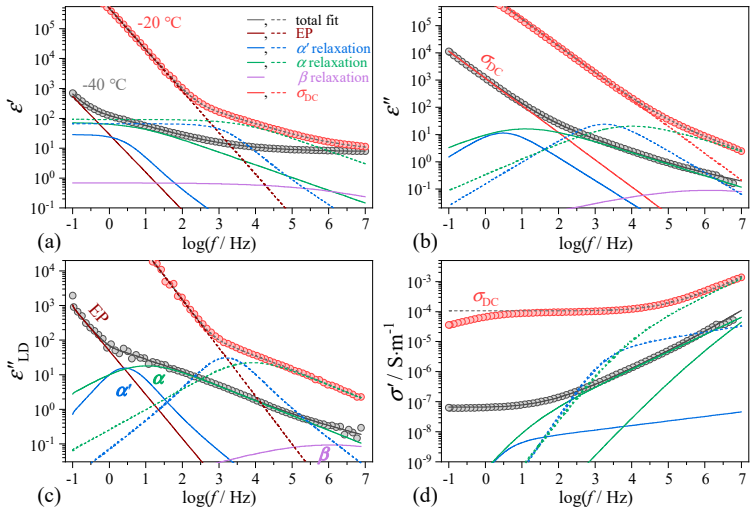

Figure 4: Spectra of dielectric constant (**a**), dielectric loss (**b**), derivative dielectric loss (**c**), and real conductivity (**d**) with fits (lines) of GPE-1 at −40°C and −20°C.

The activation behaviors of the observed dielectric relaxations in GPE-1 are presented in Fig. 5a, in which the most probable relaxation times of these relaxations are plotted against inverse temperature (the Arrhenius plot). The cases of the other GPE samples are presented in Fig. S3, which are quite similar to that of GPE-1. As clearly shown in Figs. 5a and S3, both the α' and α relaxations of all the GPE samples exhibit non-Arrhenius temperature dependence, indicating the cooperative nature of these dynamics. Furthermore, the temperature dependences of $\tau_{\alpha'}$ and τ_{α} are coarsely concordant, implying that these two relaxations are somehow coupled with each other. According to these results, the α' relaxation is not possibly attributed to interfacial polarization (which normally follows the Arrhenius law), but is most likely associated with the orientational polarization of ion-associated species as mentioned above; and the α relaxation can be assigned to the segmental dynamics of the crosslinked cellulose. The relaxation time of the β relaxation shows an Arrhenius type temperature dependence, confirming its secondary relaxation identity. Since this relaxation at most investigated temperature points shifted outside of the investigated frequency window, it will not be discussed hereinafter.

The temperature dependences of $\tau_{\alpha'}$ and τ_{α} of all investigated GPE samples are compared in Fig. 5b and Fig. 5c, respectively, which clearly reveal that both dynamics have apparent dependence on crosslinking density and lithium salt concentration. The Vogel-Fulcher-Tammann (VFT) formalism was accordingly employed to fit their non-Arrhenius temperature dependences [39], which is given by

$$\log_{10} \tau_{\max} = A + B/(T - T_0) \tag{4}$$

where A and B are constants and T_0 is the Vogel-Temperature. The VFT fitting variables of the structural α relaxation are summarized in Table S2, by which the dielectric glass transition temperature ($T_{\text{g-diele}}$) and the kinetic fragility index (m) of these samples can be evaluated by means of the following equations [39]

$$T_{\text{g-diele}} = T_0 + \frac{B}{2 - A} \tag{5}$$

$$m = \frac{2 - A}{B}[B + T_0(2 - A)] \tag{6}$$

where the number 2 is a result of log(100/s) in line with a common assumption that the glass transition typically occurs when the structural relaxation time reaches 100 s.

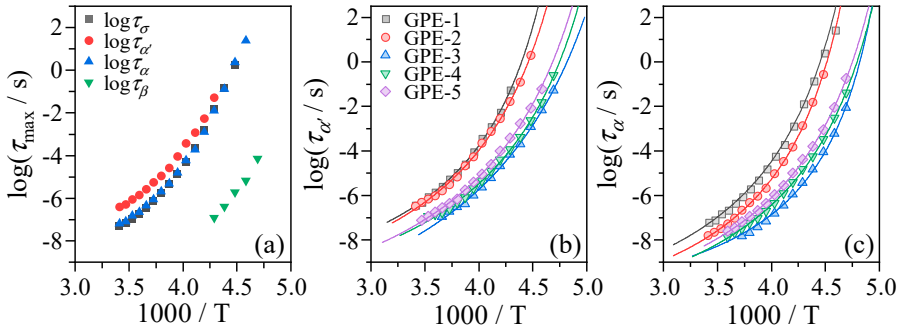

Figure 5: Temperature dependences of the relaxation time of the observed dielectric relaxations in GPE-1 (**a**), the α' relaxation (**b**), and the α relaxation (**c**) of all the GPE samples.

The dependences of $T_{g\text{-diele}}$ and m of the GPE samples on the lithium salt concentration ($n_{Li^+} : n_{AGU}$) and crosslinking density are plotted in Fig. 6, in which $T_{g\text{-DSC}}$ is also presented for comparison. Except for GPE-2, the $T_{g\text{-diele}}$ values of the other samples are apparently different from those of $T_{g\text{-DSC}}$, with the largest discrepancy approaching 15°C. The discrepancy could reflect the fact that DSC and BDS probe different manifestations of the glass transition [40], namely enthalpic recovery and structural relaxation dynamics, respectively.

While $T_{g\text{-DSC}}$ keeps within a narrow temperature range and statistically shows no apparent dependence on salt content or crosslinking density, $T_{g\text{-diele}}$ exhibits pronounced variation with these factors. At constant crosslinking density, $T_{g\text{-diele}}$ slightly decreases when $n_{Li^+} : n_{AGU}$ increases from 0.5 to 1.0, but decreases remarkably when $n_{Li^+} : n_{AGU}$ is increased to 1.5, as shown in both Figs. 5c and 6c. The shifting of $T_{g\text{-diele}}$ to lower temperature with increasing salt content may arise from several competing effects, mainly including Li^+ coordination and $TFSI^-$ plasticization. The coordination of Li^+ with the cellulose matrix brings more constraint on the segmental dynamics, and therefore tends to increase $T_{g\text{-diele}}$. On the other hand, as a well-known plasticizer due to its large size, charge delocalization, and weak coordination capability [41], $TFSI^-$ ions tend to decrease $T_{g\text{-diele}}$ through adding free volume to the cellulose matrix. When $n_{Li^+} : n_{AGU} < 1.0$, both effects may be comparable, leading to a slight decrease in $T_{g\text{-diele}}$; when $n_{Li^+} : n_{AGU} > 1.0$, however, the plasticization of $TFSI^-$ could become predominant and give rise to the obvious decrease in $T_{g\text{-diele}}$, possibly because the coordination nodes on the cellulose matrix have been saturated by Li^+. At constant salt concentration, $T_{g\text{-diele}}$ shows no monotonic dependence on the crosslinking density: a pronounced increase is observed as the crosslinking density rises from 4% to 5%, followed by a remarkable decline upon further increase to 6%. This result seems to suggest that the effect of Li^+ coordination is dominant at relatively lower crosslinking density while that of $TFSI^-$ plasticization becomes governing at higher crosslinking density.

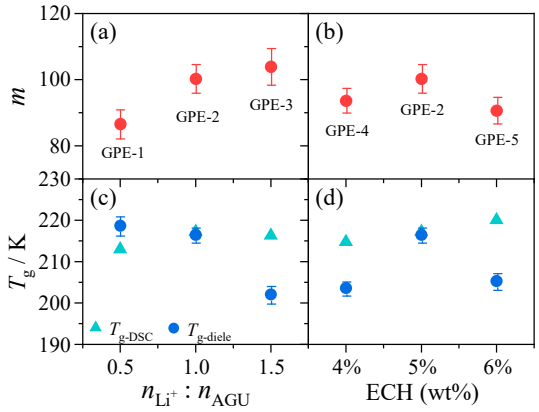

Figure 6: Kinetic fragility of the GPE samples as a function of the molar ratio of Li^+ to AGU (**a**) and crosslinking density (**b**), and dependences of their glass transition temperature on the molar ratio of Li^+ to AGU (**c**) and crosslinking density (**d**).

The kinetic fragility index, m, provides additional insight into the cooperative nature of the segmental dynamics in the investigated GPEs. As illustrated in Fig. 6, all samples exhibit m values ranging from 80 to 110, indicative of their moderately fragile glass-forming behavior [42]. For samples with the same crosslinking density, m increases monotonically with increasing $n_{Li^+} : n_{AGU}$. Although the addition of lithium salt reduces $T_{g\text{-diele}}$ and accelerates segmental dynamics, the concomitant enhancement of ion–polymer coordination and the formation of ion-associated aggregates may increase the complexity of the local dynamic landscape of the cellulose matrix. Consequently, the temperature dependence of the structural relaxation becomes more pronounced, resulting in higher fragility. In contrast, the dependence of m on crosslinking density is non-monotonic. At a constant salt concentration, the fragility first rises with increasing crosslinking density before declining at higher degrees of crosslinking. This behavior suggests a competition between enhanced cooperative rearrangements and the topological constraints imposed by the crosslinked network. Moderate crosslinking promotes collective segmental motion by increasing the cooperativity of molecular rearrangements, leading to higher fragility. However, further increment of the crosslink density suppresses large-scale cooperative motion and spatially confines chain dynamics, thereby reducing the temperature sensitivity of the relaxation process and yielding a reduction in fragility. Similar topology-dependent fragility evolution has been reported in various network-forming glassy systems, where the competition between cooperative molecular rearrangements and network constraints can lead to non-monotonic variations in fragility [43,44].

3.3 Ionic Conduction Behavior

The temperature dependences of σ_{DC} for the investigated GPE samples are plotted in Fig. 7a. The pronounced curvature observed in these profiles indicates that the ion transport in the investigated GPEs deviates from a simple thermally activated mechanism. Instead, the behavior aligns with the typical conduction patterns of GPEs where ion transport is generally regulated with segmental motions of the polymer host [22,23]. At 20°C, the samples' ionic conductivity can reach values ranging from 0.05 to 0.73 S/m, a performance level deemed highly satisfactory for energy storage applications. Besides, σ_{DC} shows apparent dependence on both salt concentration and crosslinking density, and the dependences are similar to those of the $\tau_{\alpha'}$ and τ_{α}, implying a strong coupling between ion conduction and the dynamics of cellulose matrix. It should be noted that although residual NaCl possibly exists as suggested by the XRD characterization, its contribution to the measured σ_{DC} is expected to be very limited. The presence

of NaCl diffraction peaks indicates that a considerable fraction of NaCl exists as a crystalline phase with restricted ionic mobility rather than as dissociated ions within the polymer matrix. Moreover, the systematic evolution of σ_{DC} with LiTFSI concentration and crosslinking density suggests that Li^+ ions derived from LiTFSI constitute the primary charge carriers governing the ionic transport. Therefore, any residual NaCl, if present, is expected to contribute only a marginal background signal without affecting the overall transport mechanism discussed in this work.

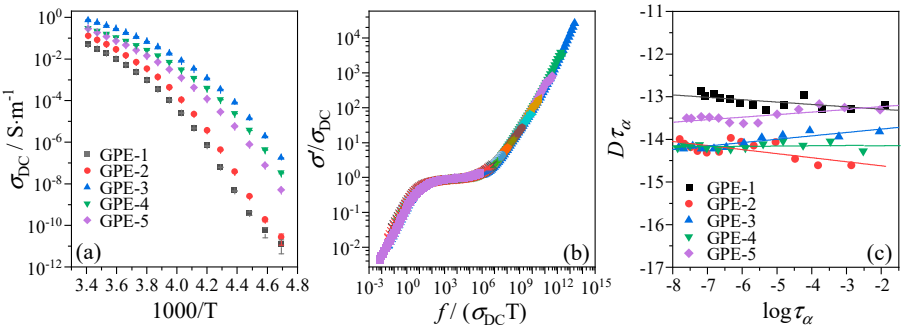

Figure 7: (**a**) Temperature dependence of DC conductivity of the investigated GPE samples; (**b**) conductivity scaling using Summerfield scaling approach for GPE-1; (**c**) $D\tau_\alpha$ as a function of log τ_α for the investigated GPE samples. The solid lines are linear fits.

The conductivity relaxation time (τ_σ) is thus compared with $\tau_{\alpha'}$ and τ_α in Figs. 5a and S3, which can be estimated from σ_{DC} via $\tau_\sigma = \varepsilon_0\varepsilon_s/\sigma_{DC}$ with ε_s being the static dielectric constant [35,45]. Remarkably, τ_σ almost perfectly coincides with τ_α over the entire investigated temperature range for all samples. Given that the α relaxation originates from the cooperative segmental motion of the crosslinked cellulose network, the close correspondence between τ_σ and τ_α provides compelling evidence that ionic conduction is strongly coupled to polymer segmental dynamics. In other words, long-range Li^+ ion transport is predominantly assisted by the local rearrangement of polymer chain segments within the investigated composition range. In contrast, although the α' relaxation exhibits a temperature dependence similar to that of the α relaxation, $\tau_{\alpha'}$ remains substantially longer than τ_σ, suggesting that the α' process does not directly govern long-range ionic transport. Instead, it is more plausibly associated with the orientational polarization of transient ionic aggregates, whose dynamics are coupled to but distinct from the charge-transport process.

Further insight into the conduction mechanism was obtained from the conductivity scaling analysis. As shown in Fig. 7b (for GPE-1) and Fig. S4 (for the other GPE samples), the frequency dependent conductivity spectra measured at different temperatures can be successfully superimposed onto a single master curve using the Summerfield scaling formalism given by [46–48]

$$\frac{\sigma'(f)}{\sigma_{DC}} = F\left(\frac{f}{\sigma_{DC}T}\right) \tag{7}$$

where F is the temperature independent scaling function. The excellent collapse of the conductivity spectra indicates that the fundamental transport mechanism remains unchanged throughout the investigated temperature range. Together with the overlap of τ_σ with τ_α, the results reveal a strong coupling between polymer dynamics and ionic transport and highlight the critical role of segmental motion in controlling the conduction behavior of crosslinked cellulose-based GPEs. In other words, the ionic conduction in the present GPEs is governed by a single segmental-motion-assisted transport mechanism over the entire temperature range investigated. In this connection, the Stokes-Einstein relationship [29,49] should be

satisfied, which indicates that the ionic diffusion coefficient D should be inversely proportional to the cellulose segmental friction η_s and τ_α, namely $D \propto T/\eta_s \propto 1/\tau_\alpha$. The ionic diffusion coefficient can be estimated from the EP effect in line with the Trukhan model [25,49,50]

$$D = \frac{2\pi f_{\max} L^2}{32(\tan\delta)^2_{\max}} \tag{8}$$

where $(\tan\delta)_{\max}$ is the maximum value of $\varepsilon''/\varepsilon'$ in the frequency range of EP, $f_{\max}$ is the frequency corresponding to the $(\tan\delta)_{\max}$, and L is the sample thickness. Fig. 7c shows the product of τ_α with the estimated D ($D\tau_\alpha$) as a function of logarithmic τ_α. As can be seen, $D\tau_\alpha$ keeps roughly constant with a slope within a range of −0.09 to 0.08, which is further evidence that ionic conduction is strongly coupled with the segmental dynamics of the crosslinked cellulose.

4 Conclusion

The present work provides a dynamic perspective on the ion transport and dielectric relaxations in crosslinked cellulose-based GPEs through an integrated approach combining BDS with structural and thermal characterizations. The structural characterization confirms the successful incorporation and coordination of lithium salts within the amorphous, crosslinked cellulose network. Three dielectric relaxations are identified across all the investigated GPE samples: a near-Debye α' relaxation associated with the collective reorientational motion of transient ionic aggregates; a structural α relaxation arising from the segmental dynamics of the crosslinked cellulose matrix; and a typical secondary β relaxation attributed to the localized side-group motions. The temperature dependence of the α' process indicates that it is governed by similar underlying glassy dynamics as the polymer matrix, while its slower timescale suggests a distinct origin associated with orientational polarization of ion-associated species.

The combined analyses of the conductivity relaxation time, Summerfield scaling of conductivity spectra, and the Stokes-Einstein relationship reveal that a singular, dominant transport mechanism prevails across the investigated temperature range. A strong correlation between the conductivity relaxation and the structural α relaxation indicates that Li^+ transport is intimately coupled to the segmental dynamics of the cellulose network. Consequently, ionic conduction in the investigated GPE samples proceeds through a segmental-motion-assisted mechanism, rather than a dynamically decoupled ion-hopping process. Furthermore, variations in lithium salt concentration and crosslinking density primarily modulate the characteristic transport timescale by altering polymer mobility, instead of inducing a mechanistic transition between different conduction pathways.

Collectively, these results establish a unified dynamic framework wherein polymer segmental motion governs Li^+ transport, while ion-associated structures give rise to additional dielectric relaxation phenomena. This work provides fundamental insight into the intricate interplay among polymer network structure, molecular dynamics, and ionic conduction, and thereby offers valuable guidance for the rational design of high-performance, sustainable cellulose-based polymer electrolytes.

Acknowledgement: Not applicable.

Funding Statement: This research was funded by the National Natural Science Foundation of China, grant number 32272408.

Author Contributions: The authors confirm contribution to the paper as follows: conceptualization, Ruoxi Zhang, Rongzu Sun, Wei Zhou, and Zhen Chen; methodology, Ruoxi Zhang, Zhen Chen; software, Zhen Chen; validation,

Ruoxi Zhang, Zhen Chen, and Rongzu Sun; formal analysis, Ruoxi Zhang, Zhen Chen; investigation, Ruoxi Zhang, Rongzu Sun, and Zhen Chen; resources, Zhen Chen; data curation, Ruoxi Zhang, Rongzu Sun; writing—original draft preparation, Ruoxi Zhang, Zhen Chen; writing—review and editing, Ruoxi Zhang, Rongzu Sun, Wei Zhou, and Zhen Chen; supervision, Zhen Chen, Wei Zhou; project administration, Zhen Chen, Wei Zhou; funding acquisition, Zhen Chen. All authors reviewed and approved the final version of the manuscript.

Availability of Data and Materials: The data that support the findings of this study are available from the Corresponding Author, ZC, upon reasonable request.

Ethics Approval: Not applicable.

Conflicts of Interest: The authors declare no conflicts of interest.

Supplementary Materials: The supplementary material is available online at https://www.techscience.com/doi/10.32604/jpm.2026.087360/s1.

References

1. Tarascon JM, Armand M. Issues and challenges facing rechargeable lithium batteries. Nature. 2001;414(6861):359–67. [CrossRef].
2. Simon P, Gogotsi Y. Materials for electrochemical capacitors. Nat Mater. 2008;7(11):845–54. [CrossRef].
3. Xu K. Electrolytes and interphases in Li-ion batteries and beyond. Chem Rev. 2014;114(23):11503–618. [CrossRef].
4. Truong KL, Bae J. Towards fire-safe polymer electrolytes for lithium-ion batteries: Strategies for electrolyte design and structural design. Polymers. 2025;17(21):2828. [CrossRef].
5. Armand M, Tarascon JM. Building better batteries. Nature. 2008;451(7179):652–7. [CrossRef].
6. Zhao Q, Stalin S, Zhao CZ, Archer LA. Designing solid-state electrolytes for safe, energy-dense batteries. Nat Rev Mater. 2020;5(3):229–52. [CrossRef].
7. Janek J, Zeier WG. A solid future for battery development. Nat Energy. 2016;1:16141. [CrossRef].
8. Aruchamy K, Ramasundaram S, Divya S, Chandran M, Yun K, Oh TH. Gel polymer electrolytes: Advancing solid-state batteries for high-performance applications. Gels. 2023;9(7):585. [CrossRef].
9. Famprikis T, Canepa P, Dawson JA, Islam MS, Masquelier C. Fundamentals of inorganic solid-state electrolytes for batteries. Nat Mater. 2019;18(12):1278–91. [CrossRef].
10. Wang C, Fu K, Kammampata SP, McOwen DW, Samson AJ, Zhang L, et al. Garnet-type solid-state electrolytes: Materials, interfaces, and batteries. Chem Rev. 2020;120(10):4257–300. [CrossRef].
11. Li Z, Fu J, Zhou X, Gui S, Wei L, Yang H, et al. Ionic conduction in polymer-based solid electrolytes. Adv Sci. 2023;10(10):e2201718. [CrossRef].
12. Han C, Shui X, Chen G, Xu G, Ma J, Dong S, et al. Recent progress in gel polymer electrolyte for lithium metal batteries. Giant. 2024;20:100337. [CrossRef].
13. Baskakova YV, Yarmolenko OV, Efimov ON. Polymer gel electrolytes for lithium batteries. Russ Chem Rev. 2012;81(4):367–80. [CrossRef].
14. Chae W, Kim B, Ryoo WS, Earmme T. A brief review of gel polymer electrolytes using *in situ* polymerization for lithium-ion polymer batteries. Polymers. 2023;15(4):803. [CrossRef].
15. Zhang J, Liu J, Xu Z, Cao D, Chen K. Enabling a sustainable future energy storage with cellulose-based solid-state electrolytes: A review. Mater Today Energy. 2025;54:102091. [CrossRef].
16. Low FS, Yabu H, Awang Selan A, Tan WC, Sun D, Thiam HS, et al. Cellulose derivation and its application for sustainable lithium-ion and emerging energy-storage systems: An overview. J Power Sources. 2026;662:238796. [CrossRef].
17. Zampieri M, Tommasone G, Morel L, Luque GL. Cellulose-based materials and their application in lithium-sulfur batteries. Polymers. 2025;17(2):164. [CrossRef].
18. Hadad S, Hamrahjoo M, Dehghani E, Salami-Kalajahi M, Eliseeva SN, Moghaddam AR, et al. Cellulose-based solid and gel polymer electrolytes with super high ionic conductivity and charge capacity for high performance lithium ion batteries. Sustain Mater Technol. 2022;33:e00503. [CrossRef].

19. Gong X, Wang J, Zhong L, Qi G, Liu F, Pan Y, et al. Recent advances on cellulose-based solid polymer electrolytes. Ind Chem Mater. 2025;3(1):31–48. [CrossRef].
20. Du X, Zhang Z, Liu W, Deng Y. Nanocellulose-based conductive materials and their emerging applications in energy devices—A review. Nano Energy. 2017;35:299–320. [CrossRef].
21. Zhang Z, Cui K, Zhang JM, Xu Y, Xu F. Cellulose-based solid-state electrolytes for solid-state lithium metal batteries: Advances in functionalization strategies and interfacial engineering. Adv Energy Mater. 2026;16(9):e04386. [CrossRef].
22. Fenton DE, Parker JM, Wright PV. Complexes of alkali metal ions with poly(ethylene oxide). Polymer. 1973;14(11):589. [CrossRef].
23. Hallinan DT Jr, Balsara NP. Polymer electrolytes. Annu Rev Mater Res. 2013;43:503–25. [CrossRef].
24. Kremer F, Schönhals A. Broadband Dielectric Spectroscopy. Berlin/Heidelberg, Germany: Springer; 2003. [CrossRef].
25. Munar A, Andrio A, Iserte R, Compañ V. Ionic conductivity and diffusion coefficients of lithium salt polymer electrolytes measured with dielectric spectroscopy. J Non Cryst Solids. 2011;357(16–17):3064–9. [CrossRef].
26. Sai Prasanna CM, Suthanthiraraj SA. Dielectric and thermal features of zinc ion conducting gel polymer electrolytes (GPEs) containing PVC/PEMA blend and EMIMTFSI ionic liquid. Ionics. 2018;24(9):2631–46. [CrossRef].
27. Ratri CR, Sabrina Q, Lestariningsih T, Nugraha AF, Astutiningsih S, Chalid M. Unveiling frequency-dependent dielectric behavior of cellulose-based polymer electrolyte at various temperature and salt concentration. Int J Renew Energy Dev. 2023;12(4):741–8. [CrossRef].
28. Patla SK, Ghosh A. Charge carrier dynamics and relaxation in highly conducting gel polymer electrolytes added with adiponitrile and dual redox. J Appl Phys. 2024;135(20):205102. [CrossRef].
29. Ngai KL. Relaxation and diffusion in complex systems. New York, NY, USA: Springer; 2011. [CrossRef].
30. Havriliak S, Negami S. A complex plane analysis of α-dispersions in some polymer systems. J Polym Sci C Polym Symp. 1966;14(1):99–117. [CrossRef].
31. Wübbenhorst M, van Turnhout J. Analysis of complex dielectric spectra. I. One-dimensional derivative techniques and three-dimensional modelling. J Non Cryst Solids. 2002;305(1–3):40–9. [CrossRef].
32. Park S, Baker JO, Himmel ME, Parilla PA, Johnson DK. Cellulose crystallinity index: Measurement techniques and their impact on interpreting cellulase performance. Biotechnol Biofuels. 2010;3:10. [CrossRef].
33. French AD. Idealized powder diffraction patterns for cellulose polymorphs. Cellulose. 2014;21(2):885–96. [CrossRef].
34. Addala S, Bouhdjer L, Chala A, Bouhdjar A, Halimi O, Boudine B, et al. Structural and optical properties of a NaCl single crystal doped with CuO nanocrystals. Chin Phys B. 2013;22(9):098103. [CrossRef].
35. Khan MA, Chen Z. New insights into the dynamics of poly(amidoamine) dendrimers with amino surface groups from segmental relaxation and ionic conductivity. Macromolecules. 2024;57(13):6199–208. [CrossRef].
36. Chen Z, Li XW, Zhao KS, Xiao JX, Yang LK. Dielectric spectroscopy investigation on the interaction of poly(diallyldimethylammonium chloride) with sodium decyl sulfate in aqueous solution. J Phys Chem B. 2011;115(19):5766–74. [CrossRef].
37. Maxwell JC. A Treatise on Electricity and Magnetism. Wotton-under-Edge, UK: Clarendon Press; 1873. [CrossRef].
38. Wagner KW. Dielektrische eigenschaften von verschiedenen isolierstoffen. Arch Für Elektrotech. 1914;3(3):67–106. [CrossRef].
39. Chen Z, Richert R. Dynamics of glass-forming liquids. XV. Dynamical features of molecular liquids that form ultra-stable glasses by vapor deposition. J Chem Phys. 2011;135(12):124515. [CrossRef].
40. Jiang H, Fang W, Zhu Y, Chen Z. Dielectric relaxation and glass transition dynamics in melt-quenched ZIF-62 glass. J Chem Phys. 2026;164(13):134504. [CrossRef].
41. Hoffknecht JP, Wettstein A, Atik J, Krause C, Thienenkamp J, Brunklaus G, et al. Coordinating anions "to the rescue" of the lithium ion mobility in ternary solid polymer electrolytes plasticized with ionic liquids. Adv Energy Mater. 2023;13:2202789. [CrossRef].
42. Angell CA. Formation of glasses from liquids and biopolymers. Science. 1995;267(5206):1924–35. [CrossRef].
43. Sidebottom DL. Connecting glass-forming fragility to network topology. Front Mater. 2019;6:144. [CrossRef].
44. Ciarella S, Biezemans RA, Janssen LMC. Understanding, predicting, and tuning the fragility of vitrimeric polymers. Proc Natl Acad Sci U S A. 2019;116(50):25013–22. [CrossRef].

45. Cao W, Gerhardt R. Calculation of various relaxation times and conductivity for a single dielectric relaxation process. Solid State Ion. 1990;42(3–4):213–21. [CrossRef].
46. Tripathy SN, Wojnarowska Z, Knapik J, Shirota H, Biswas R, Paluch M. Glass transition dynamics and conductivity scaling in ionic deep eutectic solvents: The case of (acetamide + lithium nitrate/sodium thiocyanate) melts. J Chem Phys. 2015;142(18):184504. [CrossRef].
47. Schrøder TB, Dyre JC. Scaling and universality of ac conduction in disordered solids. Phys Rev Lett. 2000;84(2):310–3. [CrossRef].
48. Summerfield S. Universal low-frequency behaviour in the a.c. hopping conductivity of disordered systems. Philos Mag B. 1985;52(1):9–22. [CrossRef].
49. Wang Y, Agapov AL, Fan F, Hong K, Yu X, Mays J, et al. Decoupling of ionic transport from segmental relaxation in polymer electrolytes. Phys Rev Lett. 2012;108(8):088303. [CrossRef].
50. Sørensen TS, Compañ V. Complex permittivity of a conducting, dielectric layer containing arbitrary binary Nernst–Planck electrolytes with applications to polymer films and cellulose acetate membranes. J Chem Soc Faraday Trans. 1995;91(23):4235–50. [CrossRef].